



# Role of Austenite Stability in Elevated Temperature Mechanical Properties of Gas Metal Arc-Directed Energy Deposition Austenitic Stainless Steels

OLIVIA DENONNO,<sup>1</sup> JUAN FELIPE GONZALES,<sup>1</sup> STEPHEN TATE,<sup>2</sup>  
ROBERT HAMLIN,<sup>3</sup> and JONAH KLEMM-TOOLE <sup>1,4</sup>

1.—Colorado School of Mines, Golden, CO 80401, USA. 2.—Electrical Power Research Institute, Charlotte, NC 28262, USA. 3.—Naval Nuclear Laboratory, Niskayuna, NY 12309, USA. 4.—e-mail: jklemmto@mines.edu

A gas metal-directed energy deposition process was used to fabricate builds using two commercial weld fillers used in power generation applications, 16-8-2 and 316H. Microstructure stability and mechanical properties were investigated through room-temperature and elevated temperature tensile testing and creep testing at 650°C, 750°C, and 825°C. 16-8-2 exhibited reduced austenite stability which resulted in athermal martensite formation after aging at 650°C for 1000 h and strain-induced martensite formation during room-temperature tensile testing. 316H exhibited relatively higher austenite stability due to increased alloying content, resulting in no athermal martensite or strain-induced martensite. Due to lower austenite stability, ferrite formed during creep at 650°C in 16-8-2, which resulted in reduced creep life and lower creep ductility compared to 316H. At 750°C and 825°C, when ferrite is no longer thermodynamically stable, 16-8-2 exhibited longer creep life and similar creep ductility as 316H. The formation of ferrite in 16-8-2 appears to have a greater impact on creep performance than the formation of embrittling topologically close-packed phases like the  $\sigma$  phase, as 316H exhibited superior creep performance while predicted to form 14 vol.%  $\sigma$  phase at 650°C.

## INTRODUCTION

Austenitic stainless steels are commonly used in power generation applications due to a combination of good corrosion resistance, moderate strength and ductility at elevated temperatures, and good toughness over a range of temperatures. Austenitic stainless steels are considered a weldable alloy group, making them a good option for additive manufacturing (AM), which is a layer-by-layer deposition that can be equated to a multi-pass welding process. AM processes like gas metal arc-directed energy deposition (GMA-DED) can be used to produce custom and replacement parts without the need for expensive tooling or a large amount of material waste compared to traditional subtractive

manufacturing. The GMA-DED process is characterized by large build volumes, high deposition rates, and cheap wire feedstock, making it the appropriate AM process for the fabrication of power generation components.<sup>1</sup> The implementation of AM for the production of replacement parts or new fabrication components in power generation has the potential to lead to drastic reductions in cost and lead times.

Power generation components must withstand elevated temperature conditions over long service lives, indicating the importance of understanding the long-term microstructure stability and creep resistance of AM austenitic stainless steel alloys. Austenitic stainless steels are susceptible to the formation of intermetallic phases, like  $\sigma$ ,  $\eta$ , and  $\lambda$  phases, during elevated temperature exposure which can embrittle the microstructure and impact the strength, toughness, and creep performance.<sup>2-4</sup> 316H is widely used in power generation

(Received November 17, 2023; accepted February 26, 2024;  
published online March 13, 2024)

applications and exhibits increased strength at elevated temperatures due to increased carbon content and greater  $M_{23}C_6$  precipitation compared to other 300 series alloys. Like many other austenitic grades, 316H is susceptible to the formation of embrittling phases, such as  $\sigma$ ,  $\eta$ , and laves.<sup>5,6</sup> To mitigate embrittling phase formation in welds, the compositionally lean weld filler metal 16-8-2 is often used. In 16-8-2, the chromium, nickel, and molybdenum contents are reduced compared to type 316H weld fillers to help prevent the formation of the  $\sigma$  phase.<sup>2,5,7</sup> 16-8-2 weld filler exhibits primary  $\delta$ -ferrite solidification which imparts solidification cracking resistance, and shows good elevated temperature creep performance from  $M_{23}C_6$  precipitation similar to 316H.<sup>4,5</sup> Due to its attractive properties, 16-8-2 is commonly used as a weld filler metal for 316H components used in higher temperature and pressure-retaining components in the petrochemical, nuclear, and power generation industries.<sup>4,5</sup> Commercial welding filler metals like 16-8-2 and 316H are the obvious starting point for material selection for the fabrication of these components using the GMA-DED process.

The thermal stability and creep resistance of 16-8-2 and 316H welds have been investigated<sup>7-11</sup> and Smith et al., summarized the effect of aging on creep properties of common 300 series filler metals. For all 300 series weld metals,  $\delta$ -ferrite forms during solidification, which is beneficial for preventing solidification cracking. However,  $\delta$ -ferrite is unstable at typical elevated temperature service conditions, resulting in the formation of carbides and intermetallic phases. Smith et al., concluded that leaner filler metals like 16-8-2 have a lower propensity for intermetallic phase formation, which promotes longer-term microstructure stability.<sup>4</sup> When producing parts with AM, solution heat treatments can be performed to dissolve the  $\delta$ -ferrite, indicating that the microstructure stability and creep performance likely differ compared to weld metal used in the as-solidified condition.

There is limited work in the literature on the creep properties and microstructure stability of AM stainless steel, with most relevant studies investigating AM 316L produced using laser powder bed fusion (L-PBF), which has a considerably different microstructure than AM 316L produced using GMA-DED. Calderon et al., compared the creep properties of L-PBF 316L to conventional hot-rolled (HR) 316L material at 600°C and 650°C. L-PBF 316L exhibited a shorter creep life and reduced creep ductility compared to HR 316L which was attributed to differences in the dislocation substructure between the AM and the wrought material.<sup>12</sup> In contrast, Li et al., found the creep ductility of L-PBF 316L to be comparable to conventional 316L at 550°C, 600°C, and 650°C, but similar to Calderon et al., with a reduced creep life. The reduced creep life of L-PBF 316L was associated with porosity and destabilization of the dislocation substructure.<sup>13</sup>

Williams et al., investigated the impact of grain orientation on the creep properties of L-PBF 316L, and found that vertically built specimens with loading parallel to the direction of columnar grain growth exhibited superior creep properties, with lower creep strain rates and longer failure times, compared to horizontally built specimens. This is expected, based on the elongated diffusion path of the columnar grains parallel to the maximum principal stress for the vertically built specimens. Creep damage was associated with build defects and porosity.<sup>14</sup> Calderon et al., summarized reported rupture times of L-PBF and wrought 316L in the literature. There is considerable spread in the data, with creep damage associated with build defects, porosity, dislocation substructure, grain and build orientation, and precipitation.<sup>12-14</sup> This indicates that more work is required to understand the creep behavior of AM stainless steel, especially since there is a lack of data on GMA-DED stainless steel.

For 16-8-2, which is designed solely as a welding feedstock, there are several reports on the influence of reduced austenite stability on the microstructure evolution of welds during high-temperature exposure. The composition of 16-8-2 is lean in alloying elements compared to other 300 series stainless steel alloys. Swanepoel et al., and Fink et al., reported athermal martensite formation in 16-8-2 weld metal after thermal aging at 750°C and 705°C, respectively.<sup>2,7</sup> Athermal martensite formation is diffusionless and depends upon undercooling below the martensite start temperature. In addition to athermal martensite formation, strain-induced martensite formation has also been reported for 16-8-2 weld metal, where externally applied stress provides the necessary mechanical driving force for martensite formation above the martensite start temperature. Lundin et al., observed a significant increase in ferrite number measured with a Feritscope after bend testing, which was associated with strain-induced martensite formation.<sup>15</sup> Hsiao observed an increase in ferrite number with increasing tensile strain for as-welded 16-8-2 tensile specimens. Carbide precipitation in specimens aged at 880°C for 0.5 h further reduced austenite stability, resulting in a greater amount of strain-induced martensite formation during tensile testing.<sup>16</sup> Recently, Gonzalez et al., showed that GMA-DED builds of 16-8-2 exhibited the formation of a considerable amount of a body centered cubic (BCC) phase during thermal aging at 650°C at 1000 h.<sup>17</sup> The formation of strain-induced martensite can result in enhanced strength and ductility under certain loading conditions, indicating that 16-8-2 could be a promising alloy for GMA-DED.

In the present work, two common commercial weld filler metals used in power generation applications, 16-8-2 and 316H, were used to produce GMA-DED builds. The elevated temperature mechanical behavior of the GMA-DED materials was investigated via room- and elevated

**Table I. As-built wall and wire composition of GMA-DED builds (wt.%)**

Materials	C	N	O	Cr	Ni	Mo	Mn	Si	P	S	Fe
316H Wire	0.05	0.05	–	18.68	11.31	2.06	1.91	0.39	0.018	0.003	Bal.
316H Build	0.05	0.064	0.039	18.79	11.30	2.11	1.81	0.34	0.017	< 0.005	Bal.
16-8-2 Wire	0.04	0.046	–	15.30	8.40	1.10	1.50	0.43	0.010	0.002	Bal.
16-8-2 Build	0.05	0.040	0.031	15.37	8.35	1.11	1.40	0.41	0.013	< 0.005	Bal.

temperature tensile testing and creep testing at 650°C, 750°C, and 825°C. Microstructure evolution resulting from exposure to 650°C for up to 1000 h and plastic deformation are characterized and discussed with respect to the differences in austenite stability between 16-8-2 and 316H. The results from this work are intended to provide a deeper understanding of the microstructure evolution reported previously by Gonzalez et al.,<sup>17</sup> and to provide insights into the effects of composition on the microstructure evolution and mechanical performance of GMA-DED stainless steels.

## EXPERIMENTAL

### Material Fabrication

A GMA-DED process was used to fabricate walls from 1.14-mm (0.045”) diameter 16-8-2 and 316H welding wire. Wire feedstock and build compositions are reported in Table I. The GMA-DED set-up is a THG Automation collaboration robot system that consists of a Universal Robot UR10e collaborative robot and a Fronius TPS 400i gas metal arc welding power source. Three-bead-wide rectangular walls approximately 254-mm long × 102-mm tall × 25-mm thick were fabricated using the cold metal transfer weld mode and a weaving weld strategy with a 3-mm pitch and 7.5-mm width. All the builds were fabricated with a travel speed of 4 mm/s (9.4 in/min), a wire feed rate of 83 mm/s (195 in/min), and a 95% Ar + 5% CO<sub>2</sub> shielding gas mixture with a flow rate of approximately 11.8 L/min (25 ft<sup>3</sup>/h).

Sections were taken from the builds and solution annealed at 1040°C for 1 h, followed by a water quench per ASTM A480/A480M.<sup>18</sup> A subset of samples received an additional 650°C aging treatment for 1000 h, followed by a water quench to mimic elevated temperature service conditions. The solution annealed and solution annealed + aged (referred hereafter to as just aged) 16-8-2 and 316H material was machined into 6.3-mm-diameter × 25.4-mm-gauge-length round tensile specimens. The additional solution-annealed 16-8-2 and 316H material was machined into 9.5-mm-diameter × 47.6-mm-gauge-length round creep samples. All tensile and creep specimens were orientated horizontal to the build direction.

Room-temperature tensile testing was performed per ASTM E8/E8M-22, and elevated tensile testing at 650°C was performed per ASTM E21-20 for all

conditions.<sup>19,20</sup> Long-term creep testing (target lifetimes of approximately 1000 h based on wrought 316H creep behavior) of the solution-annealed 16-8-2 and 316H samples was performed at 650°C at 160 MPa, 750°C at 65 MPa, and 825°C at 35 MPa using an ATS lever arm creep frame. Short-term creep testing (target lifetimes less than 500 h based on wrought 316H creep behavior) of the solution-annealed 16-8-2 and 316H samples was performed at 650°C at 185 MPa, 650°C at 200/210 MPa (16-8-2/316H), and 650°C at 245 MPa using a Zwick Roell electro-mechanical testing frame.

### Microstructure Characterization

Samples of the solution-annealed and aged 16-8-2 and 316H material were characterized using electron backscatter diffraction (EBSD), which was performed using a Helios NanoLab 600i scanning electron microscope (SEM) equipped with an EDAX Hikari Super detector with a 20-kV accelerating voltage. Failed tensile and creep samples were sectioned in the gauge length and characterized using EBSD, after which the samples were swab-etched using glyceresia (3:2:1 glycerine:HCl:HNO<sub>3</sub>) for 2 min. Microstructure characterization of the etched samples was performed on a Tescan S8000 SEM. Bulk chemical composition was determined with optical emission spectrometry per ASTM E1086-22 and nitrogen, carbon, and oxygen content was determined with combustion and inert gas fusion per ASTM E1019-18.<sup>21,22</sup> The chemical composition results of the builds are presented in Table I along with the wire composition reported by the wire manufacturers. Oxygen content was measured for the builds but was not reported for the wire. In general, negligible changes in composition were observed between the wire and build compositions.

### Phase Stability Predictions

Phase stability as a function of temperature was determined using the single-axis equilibrium module of Thermo-Calc v.2023b using the TCFE12 v12.0 database. Single-axis equilibrium simulations were performed using the build compositions of 16-8-2 and 316H reported in Table I. Note that oxygen and sulfur were not included in the simulations. Predicted equilibrium phase amounts at 650°C, 750°C, and 825°C were used to interpret the phase stability

**Table II. Equilibrium phase amounts (volume %) predicted at 650°C, 750°C, and 825°C using bulk alloy compositions**

		Ferrite	Laves	$\eta$	$M_{23}C_6$	$\sigma$
650°C	316H	0	2.2	1.7	1.0	13.4
	16-8-2	9.8	1.0	1.0	1.0	0
750°C	316H	0	0	1.4	1.0	11.5
	16-8-2	0	0	0.6	0.9	0
825°C	316H	0	0	0.8	0.9	5.9
	16-8-2	0	0	0	0.8	0

and microstructure evolution during creep. In addition, the predicted austenite composition at 650°C was used to understand changes to the austenite stability after aging.

## RESULTS

### Predicted Elevated Temperature Phase Stability

The results from the single-axis equilibrium simulations are shown in Table II for the aging and creep-testing temperatures. The equilibrium phase fraction diagrams are shown in Fig. S1 of the Supplemental Material (refer to online supplementary material). At 650°C for 16-8-2, ferrite is predicted to be stable along with  $M_{23}C_6$  carbides and intermetallic laves and  $\eta$  phases. Ferrite,  $M_{23}C_6$ , laves, and  $\eta$  are also expected to form in the aged 16-8-2 microstructure during long-term creep. No ferrite is predicted to be stable at 650°C for 316H, but a considerable amount of  $\sigma$  phase is expected to form owing to the increased alloying content of 316H. 16-8-2 is designed specifically to be lean in alloying elements to prevent the formation of the  $\sigma$  phase at elevated temperatures, while still retaining strength through  $M_{23}C_6$  precipitation.<sup>7</sup> The stability of ferrite at 650°C was unexpected, but can be rationalized by the lean alloy composition. At 750°C and 825°C, ferrite is no longer predicted to be stable in 16-8-2. During long-term creep of 16-8-2, it is anticipated that ferrite will form at 650°C, but not at 750°C or 825°C, leading to potential changes in creep properties.

### Solution Annealed and Aged Microstructure

Phase maps of the solution-annealed and aged 16-8-2 and 316H are shown in Fig. 1. Residual  $\delta$ -ferrite from the deposition process is observed for the solution-annealed conditions of 16-8-2 (Fig. 1a) and 316H (Fig. 1c). The presence of  $\delta$ -ferrite indicates that 1 h at 1040°C results in the incomplete dissolution of the  $\delta$ -ferrite that formed during solidification. After aging at 650°C for 1000 h, a large increase in the amount of a BCC phase is observed in the aged 16-8-2 condition (Fig. 1b), while no BCC phase is observed in the aged 316H condition (Fig. 1d). The increase in

BCC phase amount in the aged 16-8-2 condition is likely due to the formation of athermal martensite during cooling after the aging heat treatment, which has been reported elsewhere.<sup>2,7,15,17</sup>  $M_{23}C_6$  and other phase precipitation at the grain boundaries during aging depletes solute elements like chromium, molybdenum, and carbon from the austenite matrix, raising the martensite start ( $M_s$ ) temperature and leading to the formation of athermal martensite upon cooling.<sup>3,23</sup> In addition to athermal martensite, it is possible that ferrite forms isothermally at 650°C in 16-8-2, as approximately 9.8 vol.% is stable according to the equilibrium phase predictions shown in Table II. Despite there being a greater amount of secondary phases predicted to be stable in 316H at 650°C, no BCC phase formation was observed.

### Tensile Behavior

Representative tensile curves for 16-8-2 and 316H tested at room temperature and 650°C are shown in Fig. 2. Similar elevated tensile behavior is observed between the 16-8-2 and 316H samples, with similar yield strength and elongation reported in Table SI in the Supplementary Material. The reported tensile strength is slightly higher for the 316H samples at 650°C compared to 16-8-2. For the room-temperature tensile tests, the solution-annealed and aged 16-8-2 samples exhibit drastically different strain-hardening behavior compared to the 316H samples. The increase in the strain-hardening rate of the 16-8-2 samples indicates the formation of strain-induced martensite. The transformation of austenite to martensite during deformation is commonly referred to as the transformed induced plasticity (TRIP) effect.<sup>24</sup> In the case of the aged 16-8-2 sample tested at room temperature, the formation of strain-induced martensite occurs at a smaller strain compared to the solution-annealed sample, resulting in a higher ultimate tensile strength but a lower total elongation. The samples of 316H exhibit tensile deformation behavior consistent with a more stable austenite composition where negligible strain-induced martensite is expected. The formation of strain-induced martensite results in higher tensile strengths for the 16-8-2 samples compared to the 316H samples.

EBSD phase maps from the gauge section of failed tensile specimens are shown in Fig. 3. An increase in BCC phase amount is observed for the solution-annealed and aged 16-8-2 samples after room-temperature tensile testing. For the solution-annealed condition, an increase from 3.5% BCC (Fig. 1a) to 44.9% BCC (Fig. 3a) is observed, while, for the aged condition (Fig. 3b), the microstructure consists of almost entirely of BCC (92.3%) after tensile testing. The increase in BCC phase amount after room-temperature tensile testing provides microstructural evidence for the formation of strain-induced martensite, which is consistent with the tensile behavior of the 16-8-2 samples shown in Fig. 2a.



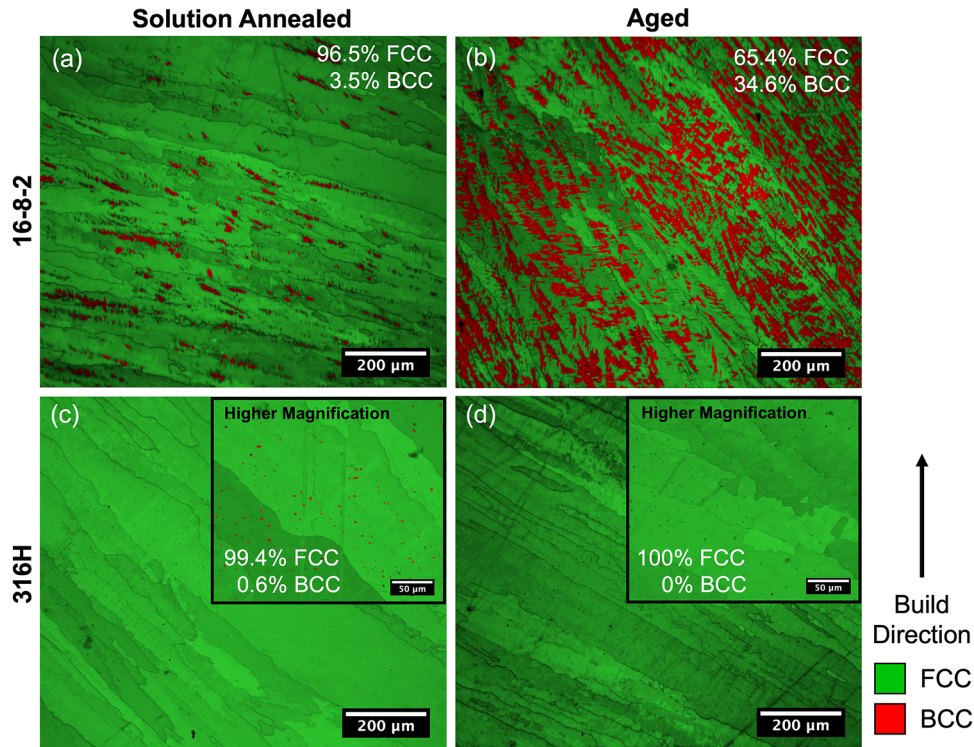


Fig. 1. Phase maps of (a) solution annealed 16-8-2, (b) aged 16-8-2, (c) solution-annealed 316H, and (d) aged 316H. Note the higher magnification phase maps for (c) and (d).

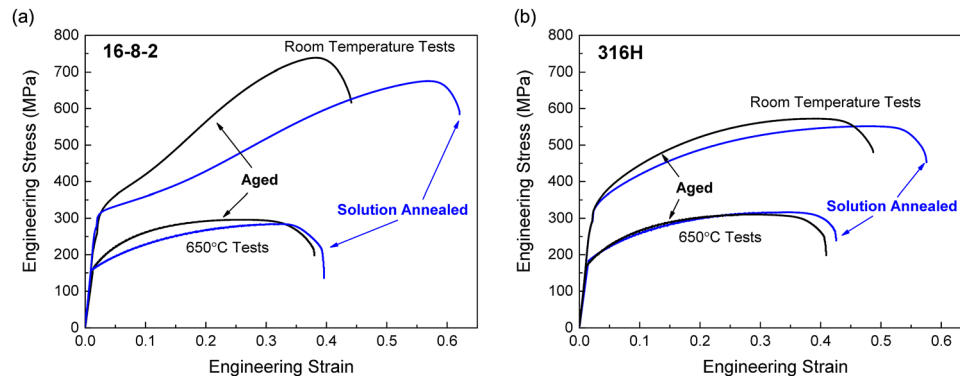


Fig. 2. Engineering stress–strain data for room temperature and 650°C tensile tests of (a) 16-8-2 and (b) 316H.

After tensile testing at 650°C, there is minimal change in the amount of BCC phase in the microstructure of the 16-8-2 samples, as can be seen by comparing Figs. 1, 3d, and e. The presence of no additional BCC phase indicates no strain-induced martensite formed during plastic deformation at 650°C. The BCC phase observed in the aged 16-8-2 sample tested at 650°C is likely a result of insufficient time for the BCC phases (ferrite and martensite) formed from aging to revert to austenite during the elevated temperature test. The absence of strain-induced martensite in 16-8-2 tested at 650°C is expected, based on the strain-hardening behavior of the tensile curves in Fig. 2a.

For 316H, no considerable change is observed after room-temperature tensile testing for the

solution-annealed condition (Fig. 3c), with residual  $\delta$ -ferrite still present, as observed in Fig. 1c. Slight coarsening of the  $\delta$ -ferrite is observed after tensile testing at 650°C (Fig. 3f). No strain-induced martensite is observed in 316H, as expected based on the strain-hardening behavior of the tensile curves in Fig. 2b. Results from aged 316H samples are not shown, but no considerable change in the amount of BCC phase is observed after tensile testing.

### Creep Behavior

Creep curves of creep strain as a function of time for 16-8-2 and 316H are presented in Fig. 4. At 650°C (Fig. 4a, b and c), 16-8-2 exhibits low creep life and reduced creep ductility compared to 316H.

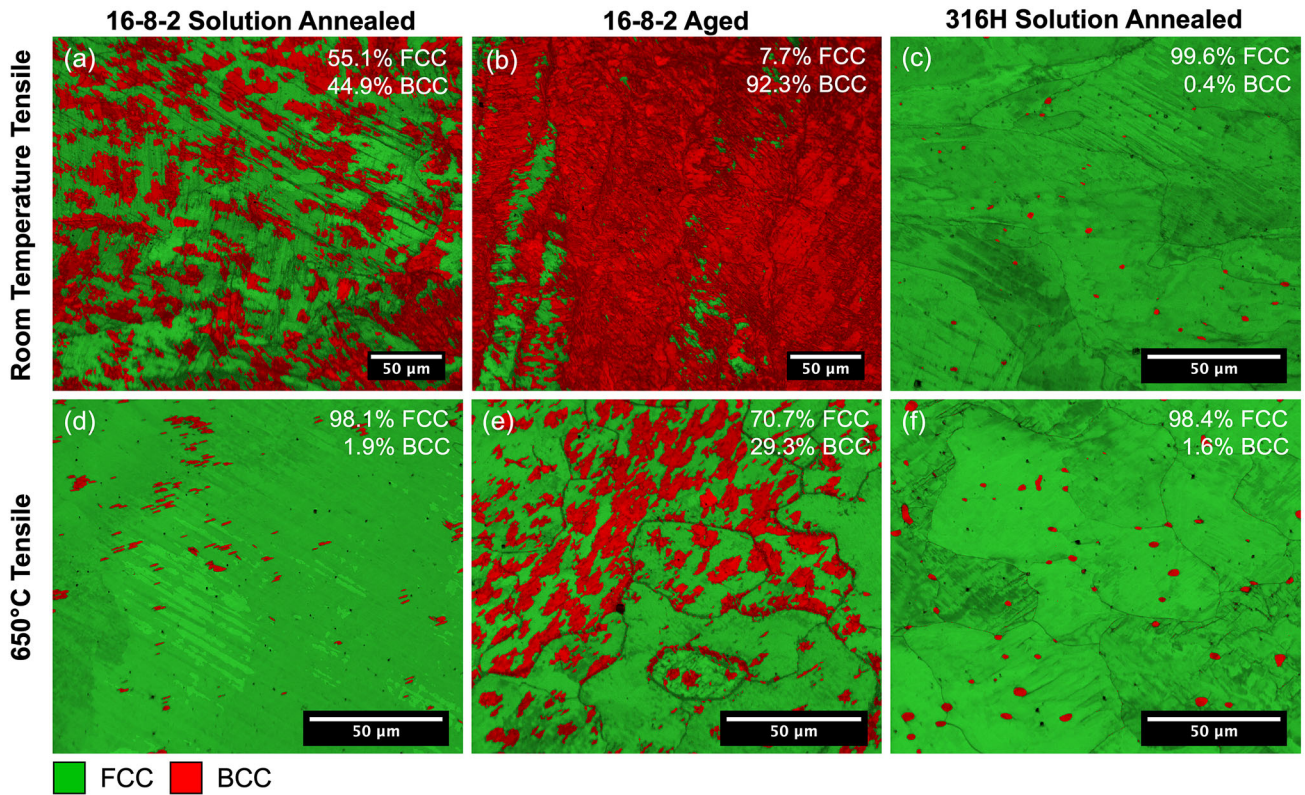


Fig. 3. EBSD phase maps from failed tensile samples: (a) solution-annealed 16-8-2 tested at room temperature; (b) aged 16-8-2 tested at room temperature; (c) solution-annealed 316H tested at room temperature; (d) solution-annealed 16-8-2 tested at 650°C; (e) aged 16-8-2 tested at 650°C; and (f) solution-annealed 316H tested at 650°C.

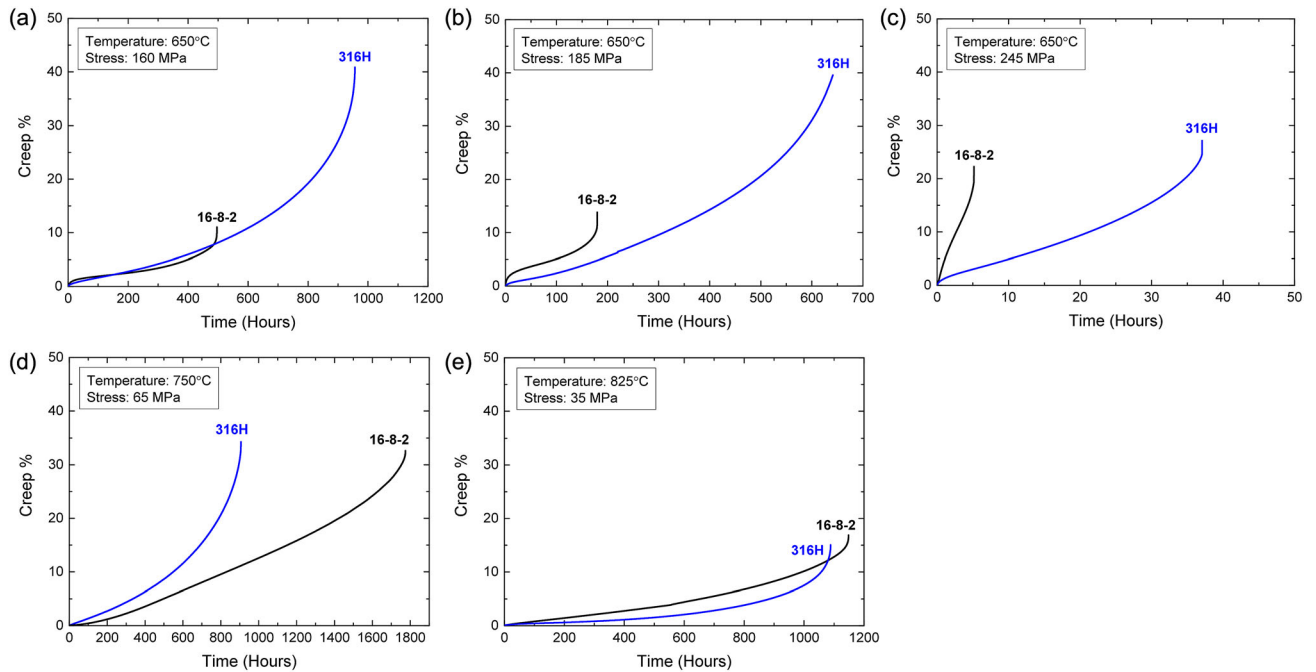


Fig. 4. Creep curves of creep strain versus time for 16-8-2 and 316H: (a) 650°C at 160 MPa; (b) 650°C at 185 MPa; (c) 650°C at 245 MPa; (d) 750°C at 65 MPa, and (e) 825°C at 35 MPa.



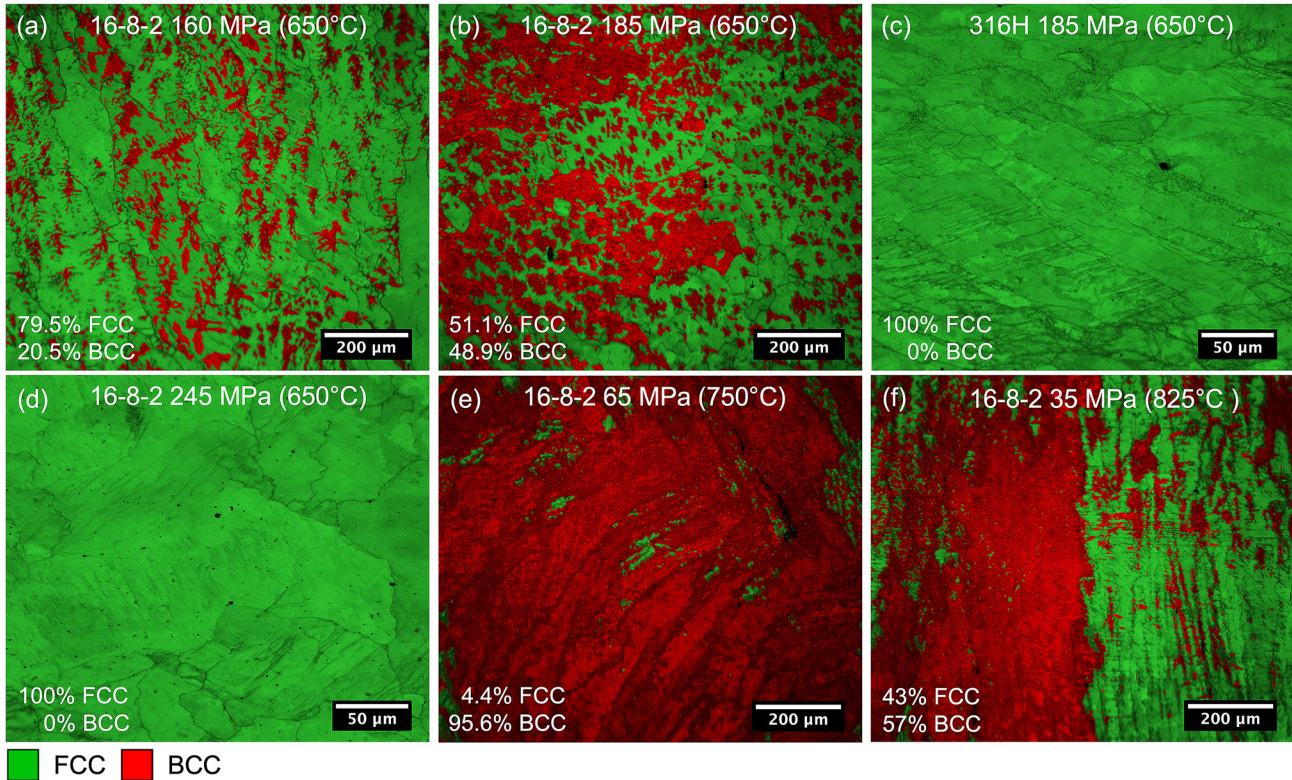


Fig. 5. EBSD phase maps from failed creep samples: (a) 16-8-2 at 160 MPa (650°C), (b) 16-8-2 at 185 MPa (650°C), (c) 316H at 185 MPa (650°C), (d) 16-8-2 at 245 MPa (650°C), (e) 16-8-2 at 65 MPa (750°C), and (f) 16-8-2 at 35 MPa (825°C).

At 750°C (Fig. 4d) and 825°C (Fig. 4e), the creep performance of 16-8-2 is considerably improved, with similar creep ductility as 316H and a longer creep life. The inferior creep performance of 16-8-2 compared to 316H at 650°C is somewhat unexpected, because the alloy is designed to avoid embrittling intermetallic phases while still having  $M_{23}C_6$  precipitation to improve creep performance. The change in relative creep performance between 16-8-2 and 316H at 650°C, 750°C, and 825°C is likely due to changes in the stability of austenite in 16-8-2. As shown in Table II, ferrite is stable at 650°C, but not at 750°C and 825°C in 16-8-2. It is possible that the formation of ferrite during creep at 650°C in 16-8-2 is responsible for the degraded creep performance.

EBSD phase maps obtained from the 16-8-2 and 316H samples after creep testing are shown in Fig. 5. Note that, prior to creep testing, all the samples were solution annealed, i.e., no creep testing of aged samples was performed. For the 16-8-2 samples tested at the lower stress values of 165 MPa (Fig. 5a) and 185 MPa (Fig. 5b), an increase in BCC phase amount is observed compared to the solution-annealed material (Fig. 1a). For the comparable 316H sample tested at 185 MPa (Fig. 5c), no increase in BCC phase is observed. No BCC is observed for the 16-8-2 sample tested at 245 MPa (Fig. 5d) which had a creep life of only

5.2 h. The BCC phase observed in 16-8-2 creep samples tested at 650°C may be a combination of ferrite that formed isothermally during the creep test and athermal martensite that formed during cooling after the test. For the 16-8-2 samples tested at 750°C (Fig. 5e) and 825°C (Fig. 5f), a large amount of BCC phase is observed. Ferrite is not stable at 750°C or 825°C (Table II), indicating that the BCC phase observed after creep testing is athermal martensite which formed upon cooling after creep testing.

Higher magnification phase maps and inverse pole figures (IPF) of two 16-8-2 creep conditions, 185 MPa (650°C) and 65 MPa (750°C), are shown in Fig. 6. The BCC phase observed in the 16-8-2 at 185 MPa (650°C) creep condition is expected to consist of ferrite and martensite, while only martensite is expected in the 16-8-2 at the 65 MPa (750°C) creep condition. High-magnification EBSD of the 185-MPa condition (Fig. 6a and c) shows BCC phase forming on austenite grain boundaries which act as preferential nucleation sites for ferrite. The austenite grain boundaries appear to be decorated with allotriomorphic ferrite, supporting the assertion the ferrite is forming isothermally at 650°C. A creep cavity is also observed at the grain boundary triple point where there is an increased stress concentration. For the 65-MPa condition (Fig. 6b and e), the austenite grain boundary does not appear to be



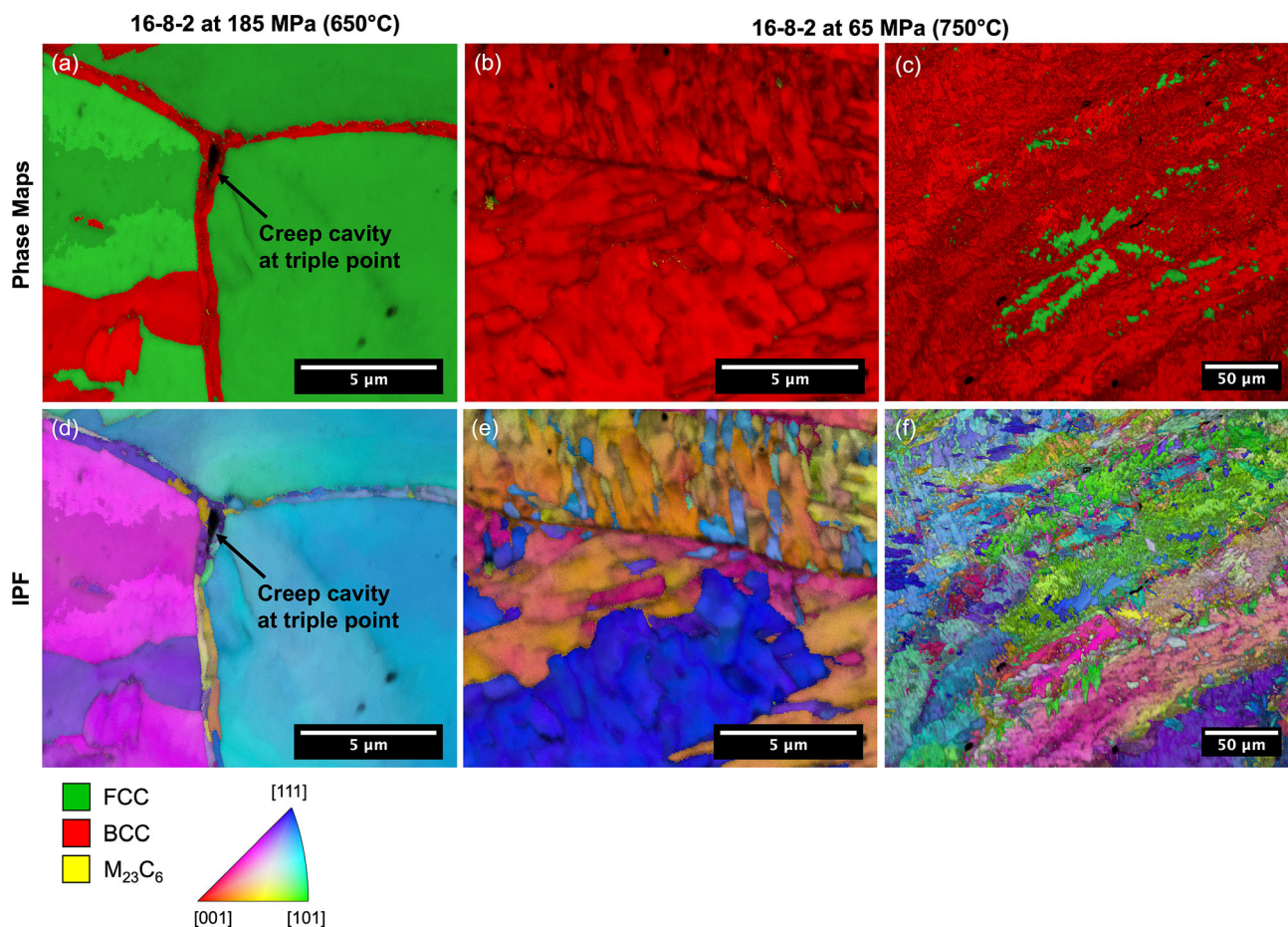


Fig. 6. Higher magnification EBSD phase maps from failed creep samples: (a) 16-8-2 at 185 MPa (650°C), (b) and (c) 16-8-2 at 65 MPa (750°C), and corresponding EBSD inverse pole figure (IPF) maps of (d) 16-8-2 at 185 MPa (650°C), (e) and (f) 16-8-2 at 65 MPa (750°C).

decorated with a BCC phase. Based on Fig. 6c and f, the BCC phase has a lath or lenticular morphology which is consistent with martensite. The morphological difference between the BCC phases present in the microstructure for the two creep conditions lends some evidence to distinguish between ferrite and martensite.

Kernel average misorientation (KAM), which evaluates local variations in misorientation between neighboring points, can be used to map plastic strain.<sup>25</sup> When comparing ferrite and martensite, it is expected that the higher dislocation density and refined substructure in martensite will exhibit increased misorientation. KAM maps of the same areas shown in Fig. 6a and b are presented in Fig. S2 of the Supplemental Material. It is observed that the “bowtie”-shaped BCC grain in Fig. 6a exhibits low KAM values, representing low local strain and indicating that it is likely ferrite, while the BCC phase in Fig. 6b exhibits increased KAM values consistent with martensite. Further work, such as dilatometry during high-temperature exposure, could be useful in proving the formation of ferrite and martensite at different temperatures. Identifying martensite variants from parent

austenite grains using IPF maps could also prove useful in distinguishing martensite from ferrite. Unlike martensite, allotriomorphic ferrite does not necessarily have an orientation relationship with the austenite grains it grows into.

Etched SEM micrographs of the corresponding creep conditions are shown in Fig. 7. Considerable secondary phase formation on grain boundaries is observed for all conditions except for the 16-8-2 sample tested at 245 MPa. The short time at elevated temperature for the 16-8-2 sample tested at 650°C at 245 MPa likely limited the degree of boundary precipitation. For all other 16-8-2 samples, the etching response of the microstructure suggests that ferrite and/or martensite is present near grain boundaries decorated with particles. This observation suggests that the formation of boundary phases such as  $M_{23}C_6$  reduces the austenite stability in 16-8-2, such that ferrite can form during creep at 650°C and that athermal martensite can also form during cooling after the creep test. For the 316H sample tested at 650°C at 185 MPa (Fig. 7c), it is observed that the grain boundaries are decorated with secondary phases. Based on the predicted equilibrium phase amounts (Table II), it is



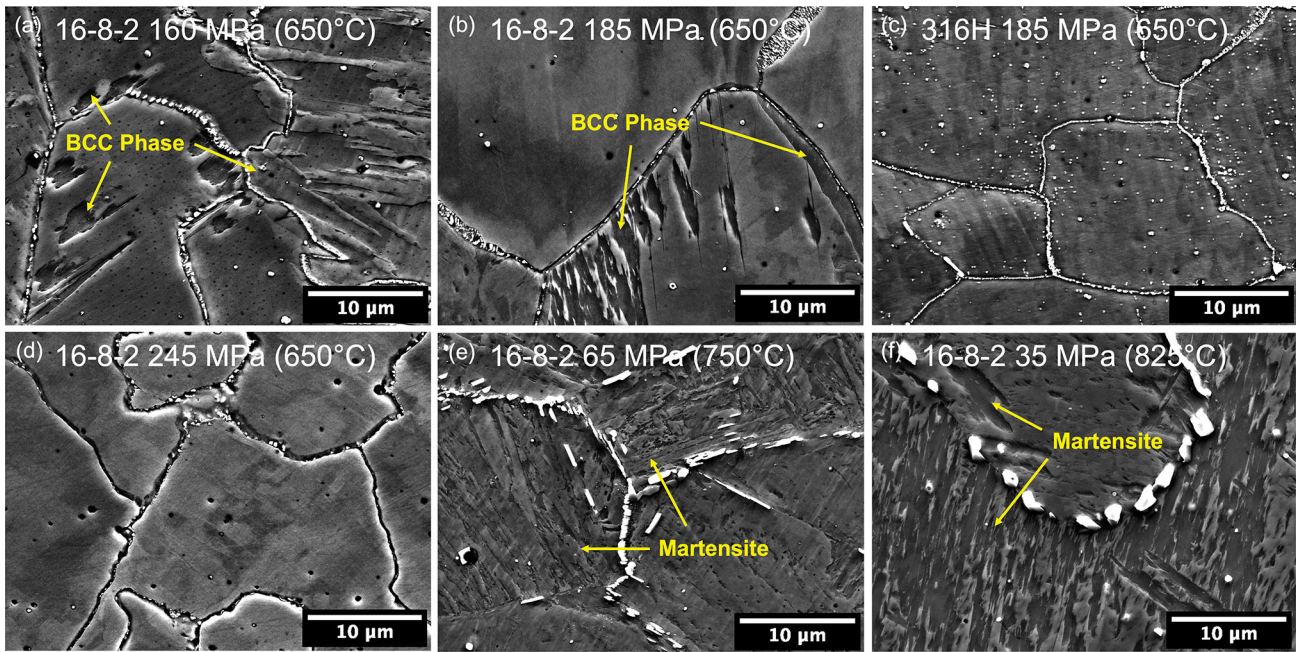


Fig. 7. Etched SEM micrographs from failed creep samples: (a) 16-8-2 at 160 MPa (650°C), (b) 16-8-2 at 185 MPa (650°C), (c) 316H at 185 MPa (650°C), (d) 16-8-2 at 245 MPa (650°C), (e) 16-8-2 at 65 MPa (750°C), and (f) 16-8-2 at 35 MPa (825°C).

likely that the grain boundaries are decorated with a majority of the  $\sigma$  phase (14 vol.% stable at 650°C), based on the size and amount of precipitates, with smaller amounts of  $M_{23}C_6$ , laves, and  $\eta$  phases possibly present as well. EBSD paired with X-ray diffraction, or transmission electron microscopy, would be needed for comprehensive characterization of the precipitates, as demonstrated in prior work.<sup>17</sup>

To further elucidate the differences in creep behavior between 16-8-2 and 316H at 650°C, a plot evaluating the stress exponent of a Norton–Bailey creep model is shown in Fig. 8.<sup>26</sup> Note that creep testing at intermediate stresses was performed for 16-8-2 and 316H to help determine the stress exponent of each material, which were not presented in Fig. 4. For all the stresses evaluated, 316H shows a stress exponent of 7.6, which is consistent with a power law glide + climb creep mechanism reported for wrought 316L.<sup>27</sup> For 16-8-2 tested at 160–200 MPa, the minimum creep rates are lower than 316H, resulting in a lower stress exponent of 5.2, which is still within the range typically associated with power law creep. The 16-8-2 sample tested at 245 MPa that failed after approximately 5 h shows a considerably higher minimum creep rate, indicating that power law breakdown occurs in 16-8-2 in the range of 200–245 MPa at 650°C. Typically lower minimum creep rates correlate with longer creep lives, assuming similar creep ductility described in the Monkman–Grant relationship.<sup>26,28</sup> Based on the minimum creep rates, 16-8-2 should have better creep performance than 316H at 650°C, but this was not observed experimentally. The creep curves shown in Fig. 4a and b indicate that, within

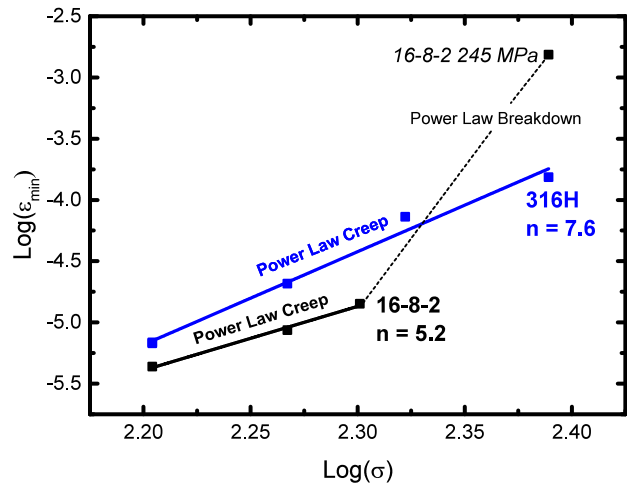


Fig. 8. Plot of  $\log(\text{stress})$  vs.  $\log(\text{minimum creep rate})$  for 16-8-2 and 316H 650°C creep samples where the slope of each linear fit is the creep exponent in the Norton–Bailey creep model.

power law creep, 16-8-2 has a lower creep ductility and creep life than 316H. It is possible that ferrite formation during creep testing in the 16-8-2 samples tested at 650°C is leading to reduced creep ductility and ultimately, and unexpectedly, low creep lives.

## DISCUSSION

### Athermal Martensite Formation in 16-8-2

Athermal martensite formation in austenitic stainless steels resulting from high-temperature exposure has been observed previously. Butler

**Table III. Bulk alloy composition and predicted austenite composition at 650°C used to calculate  $M_s$  and  $M_{d30}$  temperatures**

Materials	C	N	Cr	Ni	Mo	Mn	Si	$M_s$	$M_{d30}$
Bulk 316H	0.05	0.064	18.79	11.30	2.11	1.81	0.34	− 429°C	− 61°C
Austenite in 316H at 650°C	0.00056	0.00056	14.44	12.58	0.47	1.92	0.27	− 139°C	69°C
Bulk 16-8-2	0.05	0.040	15.37	8.35	1.11	1.40	0.41	− 54°C	46°C
Austenite in 16-8-2 at 650°C	0.00073	0.00047	14.25	8.88	0.38	1.54	0.37	105°C	110°C

et al., noted that the formation of carbides in 304 stainless steel resulted in chromium depletion near grain boundaries, which provided the necessary conditions for athermal martensite formation during cooling.<sup>23</sup> Swanepoel et al., and Fink et al., observed athermal martensite formation in 16-8-2 filler metal weld on 304H after aging. Swanepoel et al., reported martensite after aging at 750°C for 1000–3500 h, and Fink et al., reported after aging at 705°C for 168 h.<sup>2,7</sup>

The impact of compositional depletion in austenite from boundary precipitation on the martensite start temperature ( $M_s$ ) is demonstrated in Table III, where the  $M_s$  temperature is calculated for the bulk composition as well as for the predicted equilibrium austenite composition at 650°C. It is assumed that the bulk composition is representative of the austenite composition in the solution-annealed condition. The  $M_s$  temperature is calculated using the equation developed by Eichelman and Hull for calculating the  $M_s$  temperature based on the alloy composition of a nominally fully austenitic microstructure:

$$M_s(^{\circ}\text{C}) = 1305.2 - 41.7[\text{Cr}] - 61.1[\text{Ni}] - 33.3[\text{Mn}] - 27.8[\text{Si}] - 1666.7([\text{C}] + [\text{N}]) \quad (1)$$

where  $[X]$  is the wt.% of each element present in the alloy.<sup>3,29</sup> It can be seen from Eq. 1 that the reduction of alloying elements from austenite serves to decrease the austenite stability relative to the martensite, thereby increasing the  $M_s$  temperature. Unlike when considering austenite stability relative to  $\delta$ -ferrite, all alloying elements stabilize austenite with respect to martensite.<sup>30</sup>

Using the bulk 16-8-2 composition measured after deposition, the calculated  $M_s$  temperature is below room temperature. The predicted  $M_s$  temperature for the bulk composition corroborates what is observed experimentally for the solution-annealed condition where no athermal martensite formed. The equilibrium austenite composition predicted at 650°C has considerably less carbon, nitrogen, chromium, and molybdenum compared to the bulk composition, resulting in the calculated  $M_s$  temperature shifting to above room temperature. The change in austenite composition at 650°C is a result of equilibrium amounts of  $M_{23}C_6$ , ferrite,  $\eta$ , and

laves formation, which creates the necessary conditions for athermal martensite formation after aging.

The calculated  $M_s$  temperature for 316H is below room temperature based on the bulk composition and the equilibrium austenite composition at 650°C, indicating that no athermal martensite should form, which also matches what was observed experimentally. The greater amount of chromium and molybdenum in the bulk composition of 316H results in a more stable austenite composition at 650°C compared to 16-8-2, even with the predicted equilibrium amount of 14 vol.%  $\sigma$  phase in the aged condition.

The austenite compositions shown in Table III for 16-8-2 and 316H are based on equilibrium phase predictions. 16-8-2 and 316H may not have reached equilibrium at 650°C even after a 1000-h ageing, indicating that the experimental austenite compositions may vary from the predicted compositions shown in Table III. If less than the equilibrium phase fraction of secondary phases formed during aging, the austenite composition will be less “lean” than what was predicted, i.e., more carbon, nitrogen, chromium, and molybdenum are expected to stay in solution. Similarly, nickel and manganese contents may not have increased as much as predicted at 650°C. It should be noted that the reductions in carbon, nitrogen, chromium, and molybdenum content in austenite from secondary phase formation far outweigh the increases in nickel and manganese, resulting in an overall reduction in austenite stability relative to martensite.

### Strain-Induced Martensite Formation in 16-8-2

The high strain-hardening rates of the solution-annealed and aged 16-8-2 samples tested at room temperature are attributed to the formation of strain-induced martensite. An increasing strain-hardening rate with increasing plastic strain is a manifestation of strain-induced martensite formation in the TRIP effect.<sup>24,31</sup> The EBSD phase maps of the 16-8-2 samples (Fig. 3a and b) show an increase in the amount of BCC phase after room-temperature tensile testing, further indicating the formation of strain-induced martensite. For strain-induced martensite to form, plastic deformation must be applied below the  $M_d$  temperature and above the  $M_s$  temperature, where the  $M_d$



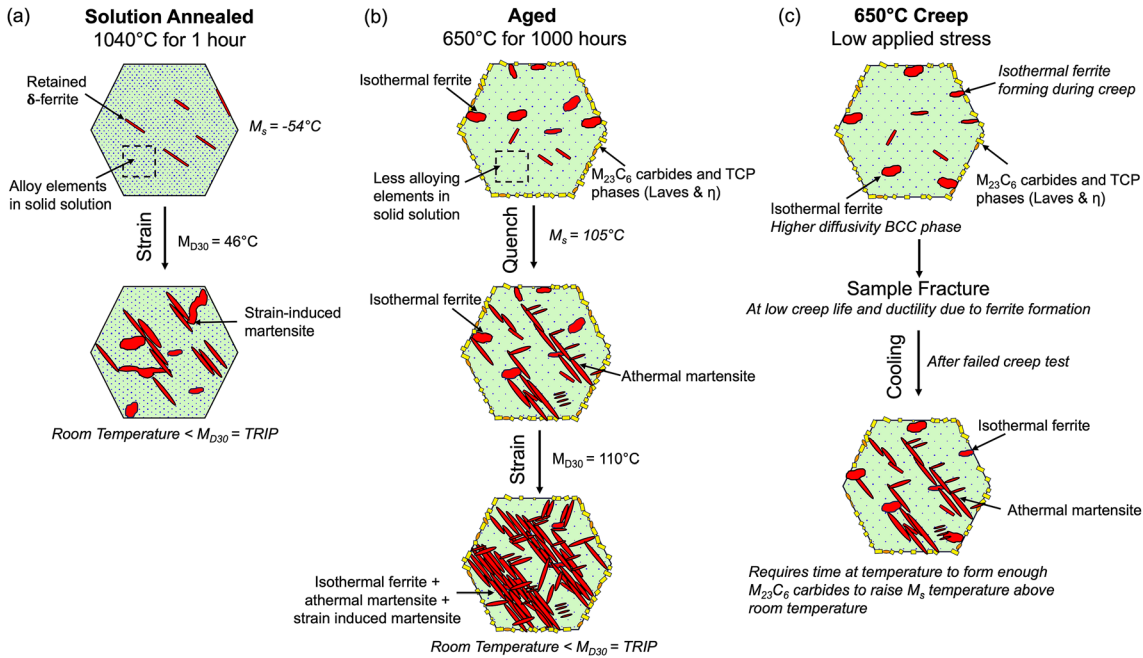


Fig. 9.. Schematic of microstructure evolution during: (a) room-temperature tensile testing of solution-annealed 16-8-2, (b) room-temperature tensile testing of aged 16-8-2, and (c) creep testing of 16-8-2 at 650°C and low applied stress.

temperature is the minimum temperature for which strain-induced martensite can form. Above the  $M_d$  temperature, no amount of plastic strain will result in a transformation.<sup>30,31</sup> The results in Figs. 2 and 3 indicate that the  $M_d$  temperature for GMA-DED 16-8-2 is above room temperature and below 650°C.

The formation of strain-induced martensite is impacted by alloy composition. Angel determined an empirical relationship between alloy composition and temperature at which 50 vol.% strain-induced martensite forms in a fully austenitic microstructure at a true tensile strain of 0.3, called the  $M_{d30}$  temperature shown in:

$$M_{d30} (^{\circ}\text{C}) = 413 - 462[\text{C} + \text{N}] - 9.2[\text{Si}] - 8.1[\text{Mn}] - 13.7[\text{Cr}] - 9.5[\text{Ni}] - 18.5[\text{Mo}] \quad (2)$$

where  $[X]$  is the wt.% of each element present in the alloy.<sup>30</sup> The lower the  $M_{d30}$  temperature, the greater the austenite stability.<sup>24</sup>

Leaner alloy compositions have a lower austenite stability and higher  $M_{d30}$  temperature, indicating a greater propensity for strain-induced martensite formation. This is demonstrated by the calculated  $M_{d30}$  temperatures for 16-8-2 and 316H presented in Table III. Using the bulk compositions of 16-8-2 and 316H, which are assumed to be representative of the austenite compositions of the respective alloys in the solution-annealed condition, the calculated  $M_{d30}$  temperature is above room temperature for 16-8-2, and below room temperature for 316H. These calculated  $M_{d30}$  temperatures match what is observed experimentally, that solution-annealed 16-8-2 exhibits strain-induced martensite formation

and solution-annealed 316H does not. When considering the aged microstructure of both alloys where the formation of  $M_{23}C_6$ , topologically close-packed (TCP) phases, and ferrite (only for 16-8-2) impacts the austenite composition, an  $M_{d30}$  temperature above room temperature has been calculated for both alloys. The higher  $M_{d30}$  temperature for aged 16-8-2 indicates a further reduction in austenite stability, which may explain the greater total amount of BCC phases observed after room-temperature tensile testing in the aged condition. For aged 316H, no strain-induced martensite was observed, even though the  $M_{d30}$  temperature is calculated to be above room temperature. This is likely, because there is a discrepancy between the equilibrium phase amounts predicted at 650°C (Table II) and the actual amount that formed. The single-axis equilibrium simulation predicts 14%  $\sigma$  phase formation at 650°C, which results in depletion of chromium and molybdenum from the austenite matrix. Based on the absence of strain-induced martensite formation for the aged 316H samples, it is likely that less than 14 vol.%  $\sigma$  phase formed during aging, and that the experimental austenite composition is not as lean as what is presented in Table III. Further characterization is needed to conclusively verify and determine the amount of  $\sigma$  phase that formed at 650°C during aging compared to equilibrium predictions.

For the 16-8-2 room-temperature tensile samples, a difference in strain-hardening behavior is observed between the solution-annealed and aged conditions (Fig. 2a). The increased strain-hardening rate for the aged 16-8-2 sample results in greater ultimate tensile strength, but reduced ductility,

compared to the solution-annealed sample. While there is a difference in the propensity for strain-induced martensite formation between the two conditions, indicated by the slightly higher  $M_{d30}$  temperature for the aged condition, a similar amount of strain-induced martensite was formed between the two conditions. Approximately 45% martensite formed in the solution-annealed condition and 55% formed in the aged condition. The difference in the starting microstructure prior to tensile testing between the solution-annealed and aged conditions may also contribute to the differences in strain-hardening behavior.

Schematics outlining the impact differences in starting microstructure of 16-8-2 solution-annealed and aged conditions had on room-temperature tensile behavior are shown in Fig. 9a and b. Athermal martensite and isothermally formed ferrite are present in the aged 16-8-2 condition, while an almost completely austenitic microstructure is observed in the solution-annealed 16-8-2 condition. As a result, the effective austenite starting grain size in the aged condition is smaller. During tensile deformation at room temperature, each incremental amount of strain-induced martensite that formed resulted in a greater reduction of overall effective grain size in the aged condition, due to the smaller starting austenite grain size. The greater reduction in overall effective grain size with a given increment of plastic strain (and amount of martensite formed) produces a greater dynamic grain size reduction effect, and therefore a higher strain-hardening rate in the aged condition of 16-8-2.

### Effects of Austenite Stability on Creep Performance

The creep performance of 16-8-2 at 650°C is inferior to that of 316H. Lower than expected creep ductility and creep life are observed for 16-8-2 at all stresses evaluated at 650°C. In contrast, the creep performance of 16-8-2 at 750°C and 825°C is comparable to that of 316H with similar creep ductility and longer creep life. The discrepancy in creep performance at 650°C points to the formation of ferrite during creep as being a possible reason for the poor creep performance of 16-8-2.

During steady-state creep, there is a balance between an increase in dislocation density from work hardening and the annihilation of dislocations through thermal recovery. As such, the creep process is dependent upon dislocation climb for the annihilation and rearrangement of dislocations.<sup>12</sup> Dislocation climb requires the diffusion of vacancies, indicating a dependency on atomic diffusion. The close-packed face-centered cubic (FCC) crystal structure of austenite has a lower diffusivity than BCC ferrite, indicating that dislocation climb is harder in austenite. Sherby and Burke showed that, at 910°C, for a given stress, the minimum creep rate of  $\alpha$ -iron (BCC) is 200 times greater than that of

$\gamma$ -iron (FCC) due to self-diffusion in  $\alpha$ -iron being 350 times greater than in  $\gamma$ -iron.<sup>32</sup> This indicates that the poor creep performance of 16-8-2 at 650°C could be due to the formation of higher diffusivity ferrite during creep. Additionally, the increased interphase boundary area between isothermally formed ferrite and austenite may act similarly to high-angle grain boundaries, further increasing the net diffusivity in the multiphase microstructure.

The formation of ferrite likely occurs after the point where the minimum creep rate is observed, i.e., during tertiary creep based on Fig. 8. The 16-8-2 samples exhibit lower minimum creep rates than the 316H samples, indicating that 16-8-2 should have increased creep life, which was not observed experimentally. In order for 16-8-2 to exhibit lower minimum creep rates but shorter creep lives than 316H, ferrite likely forms during the latter stages of tertiary creep, where there is a more rapid accumulation of plastic creep strain. If ferrite formed in earlier stages of creep, it would be expected that the minimum creep rate would be higher owing to the overall increase in diffusivity discussed above. The formation of ferrite in tertiary creep likely accelerates creep damage locally, where ferrite forms at boundaries leading to lower creep ductility and overall lower creep life.

The total amount of BCC phase(s) observed in the 16-8-2 creep samples tested at 160 MPa (Fig. 5a) and 185 MPa (Fig. 5b) at 650°C is higher than the equilibrium-predicted amount presented in Table II. The 20% and 50% BCC phase observed in the 160 MPa and 185 MPa creep samples, respectively, cannot be explained by ferrite formation alone, as only 10% is predicted to be present at equilibrium at 650°C. As already indicated, a sufficient amount of  $M_{23}C_6$ , ferrite and TCP phases formed during creep at 650°C, such that the  $M_s$  temperature of 16-8-2 samples was raised above room temperature. After the creep tests, as the samples cooled, athermal martensite formed, resulting in higher total BCC phase amounts (ferrite + martensite) than anticipated from equilibrium predictions. Note that martensite is not expected to form during creep, so it likely has no impact on the creep performance discussed above. The martensite present just impacts the post-mortem microstructure, as characterized by the EBSD analysis shown in Fig. 5.

The microstructure evolution of 16-8-2 during creep at 650°C is represented schematically in Fig. 9c. During creep, ferrite,  $M_{23}C_6$ , and TCP phases form. As noted, the increase in diffusivity as a result of ferrite formation during tertiary creep leads to premature creep failure. After the sample fails, it is cooled to room temperature during which athermal martensite forms. The formation of martensite depends on the creep life of the sample being long enough that sufficient amounts of  $M_{23}C_6$  and TCP phases form and raise the  $M_s$  temperature above room temperature. If the creep life is too short, as is the case with the 245 MPa sample



(Fig. 5d), there is not enough time to form the grain-boundary phases needed to generate the unstable austenite composition required for athermal martensite formation.

Although the 16-8-2 creep samples tested at 750°C (Fig. 5e) and 825°C (Fig. 5e) locally show 96% BCC and 57% BCC, respectively, it is likely that none of the BCC phase is isothermally formed ferrite, as supported by the morphology and location of the BCC phase shown in Fig. 6b and c. Ferrite is not stable at 750°C and 825°C according to the equilibrium phase predictions (Table II), so none of the BCC phase indexed in those phase maps is expected to be ferrite, but rather athermal martensite that formed after the creep tests. The 750°C creep sample at 65 MPa had a creep life of 1774.8 h, and the 825°C creep sample at 35 MPa had a creep life of 1148.3 h. These extended times at elevated temperatures are likely sufficient to allow for  $M_{23}C_6$  and TCP phase formation, as shown in Fig. 7e and f, to cause local compositional depletion of the austenite to raise the  $M_s$  temperature above room temperature. The creep performance of 16-8-2 at 750°C and 825°C is similar if not superior to that of 316H, likely because ferrite is not forming during creep and causing the acceleration of creep strain in tertiary creep.

The minimum creep rates of 16-8-2 and 316H at 750°C and 825°C are extremely similar, as shown in Table SII in the Supplemental Material. The similar minimum creep rate between 16-8-2 and 316H at 825°C correlates well with similar rupture times of 1148 h and 1089 h, respectively. At 750°C, the rupture times of 16-8-2 and 316H, 1775 h and 906 h, respectively, vary considerably given the similar minimum creep rates. This indicates increased damage accumulation during tertiary creep at 750°C for 316H, which is impacting the creep life. Future work analyzing creep damage for each of these conditions is needed to understand the mechanism causing variation in the rupture time, given similar minimum creep rates.

### Considerations of Austenite Stability for GMA-DED Stainless Steels in High-Temperature Structural Applications

When considering the use of GMA-DED 16-8-2 in power generation applications, the decreased austenite stability leading to the formation of multiphase microstructures is concerning, especially with respect to the degradation of creep properties when ferrite is formed. 16-8-2 is designed to be compositionally lean in order to mitigate embrittling phase formation, which results in the unintended consequence of reducing austenite stability. It appears that the formation of ferrite as a result of austenite instability is more of a concern with respect to creep performance than the formation of embrittling TCP phases, like the  $\sigma$  phase, as 316H is predicted to form 14 vol.%  $\sigma$  phase at 650°C

but exhibited superior creep performance. The decreased performance of 16-8-2 at elevated temperatures may be known, as there is a weld strength reduction factor for 316L stainless steel welded with 16-8-2 filler between 538°C and 621°C per ASME BPVC Section 1.<sup>33</sup> Future work will include a comparison of GMA-DED stainless steel (16-8-2, 316H, 316L, and 316LSi) creep performance to that of wrought stainless steel.

In addition, the formation of athermal martensite upon cooling as a result of decreased austenite stability is a concern when considering the service conditions that a power generation component may face. While athermal martensite formation does not impact creep or tensile properties at elevated service temperatures, it could have an impact if a part is cooled during service and the microstructure transforms to multiphase austenite + martensite microstructure. Swanepoel et al., and Fink et al., showed that, when martensite forms in 16-8-2 welds after aging, the impact toughness decreases.<sup>2,7</sup>

As ferrite has a larger impact on creep properties than TCP phases like the  $\sigma$  phase, there is an opportunity for alloy modification of 16-8-2 to improve creep performance, particularly at 650°C. Slight increases in alloying content to stabilize austenite while still minimizing the  $\sigma$  phase amount could lead to a modified 16-8-2 alloy that exhibits superior elevated temperature mechanical properties.

## CONCLUSION

GMA-DED builds were produced using two austenitic stainless steel compositions, 16-8-2 and 316H, with different austenite stabilities which are commonly used in high-temperature applications. The microstructure evolution of each alloy during long-term thermal aging and deformation was investigated. Room-temperature and elevated temperature tensile testing and creep testing at 650°C, 750°C, and 825°C were performed. It was observed that GMA-DED 16-8-2 has limited austenite stability compared to GMA-DED 316H, resulting in an interesting combination of tensile and creep properties. The conclusions from this study are as follows:

- Athermal martensite formation was observed in 16-8-2 after aging at 650°C for 1000 h.  $M_{23}C_6$  and other TCP phase precipitation at grain boundaries during aging depletes solute elements from the austenite matrix and raises the martensite start ( $M_s$ ) temperature. Austenite is more stable in 316H due to increased alloying content compared to 16-8-2, so no athermal martensite was formed after aging.
- Increased strain-hardening rates in the 16-8-2 samples tested at room temperature is attributed to the formation of strain-induced martensite. The leaner alloy composition of 16-8-2 has a lower austenite stability and higher  $M_{d30}$

temperature, indicating a higher propensity for strain-induced martensite formation. Strain-induced martensite results in higher tensile strengths for the 16-8-2 samples compared to the 316H samples, which did not exhibit strain-induced martensite formation at room temperature.

- 16-8-2 exhibited reduced creep life at 650°C compared to 316H due to the formation of ferrite during creep. The increased diffusivity of ferrite combined with the increased interphase boundary area between isothermally formed ferrite and austenite resulted in reduced creep lives and creep ductility. Ferrite is not stable at 750°C and 825°C, and, as a result, the creep life of 16-8-2 at 750°C and 825°C was similar if not superior to that of 316H.
- The minimum creep rates for 16-8-2 in the power law creep regime at 650°C are lower than that of 316H even though 16-8-2 exhibits reduced creep life. The lower minimum creep rates for 16-8-2 indicate that ferrite is likely forming in tertiary creep and accelerating creep damage, leading to lower creep ductility and overall lower creep life.
- The formation of ferrite in 16-8-2 as a result of lower austenite stability appears to have a greater impact on creep performance than the formation of embrittling TCP phases like the  $\sigma$  phase, as 316H exhibited superior creep performance but is predicted to form 14 vol.%  $\sigma$  phase at 650°C.

### SUPPLEMENTARY INFORMATION

The online version contains supplementary material available at <https://doi.org/10.1007/s11837-024-06489-3>.

### ACKNOWLEDGMENTS

The authors acknowledge support from the Advanced Manufacturing Methods and Materials Initiative at the Electric Power Research Institute as well as the Manufacturing and Materials Joining Innovation Center (Ma<sup>2</sup>JIC). This material is based upon work supported by the National Science Foundation under Grant Number (2052819). Data analysis was supported by instrumentation that was acquired through the support of the National Science Foundation (DMR-1828454). Any opinions, findings, and conclusions or recommendations expressed in this material are those of the author(s) and do not necessarily reflect the views of the National Science Foundation.

### AUTHOR CONTRIBUTION

Olivia DeNonno: Conceptualization, Methodology, Formal Analysis, Investigation, Writing—Original Draft, Writing—Review and Editing.

Juan Gonzales: Conceptualization, Methodology, Investigation. Stephen Tate: Conceptualization, Resources, Writing—Review and Editing, Funding Acquisition. Robert Hamlin: Writing—Review and Editing, Supervision, Funding Acquisition. Jonah Klemm-Toole: Conceptualization, Methodology, Resources, Writing—Review and Editing, Supervision, Funding Acquisition

### CONFLICT OF INTEREST

On behalf of all authors, the corresponding author states that there is no conflict of interest.

### OPEN ACCESS

This article is licensed under a Creative Commons Attribution 4.0 International License, which permits use, sharing, adaptation, distribution and reproduction in any medium or format, as long as you give appropriate credit to the original author(s) and the source, provide a link to the Creative Commons licence, and indicate if changes were made. The images or other third party material in this article are included in the article's Creative Commons licence, unless indicated otherwise in a credit line to the material. If material is not included in the article's Creative Commons licence and your intended use is not permitted by statutory regulation or exceeds the permitted use, you will need to obtain permission directly from the copyright holder. To view a copy of this licence, visit <http://creativecommons.org/licenses/by/4.0/>.

### REFERENCES

1. T. DebRoy, H.L. Wei, J.S. Zuback, T. Mukherjee, J.W. Elmer, J.O. Milewski, A.M. Beese, A. Wilson-Heid, A. De, and W. Zhang, *Prog. Mater. Sci.* 92, 112 (2018).
2. C. Fink, H. Wang, B. T. Alexandrov, and J. Penso, *WJ* 99, 312 (2020).
3. A.F. Padilha and P.R. Rios, *ISIJ Int.* 42, 325 (2002).
4. J.J. Smith and R.A. Farrar, *Int. Mater. Rev.* 38, 25 (1993).
5. American Welding Society (AWS) A5 Committee on Filler Metals and Allied Materials, *Welding Consumables—Wire Electrodes, Strip Electrodes, Wires, and Rods for Arc Welding of Stainless and Heat Resisting Steels—Classification* (2016).
6. W. Ren and L. Lin, in *ASME 2019 Pressure Vessels & Piping Conference* (ASME, 2019).
7. D.B. Swanepoel and P.G.H. Pistorius, *Weld World* 66, 301 (2022).
8. R.L. Klueh and D.P. Edmonds, *Weld. J.* 65, 156 (1986).
9. S. Wei, L. Zhao, D. Gao, and S. Lu, *Mater. Sci. Technol.* 36, 793 (2020).
10. A.D. Warren, I.J. Griffiths, R.L. Harniman, P.E.J. Flewitt, and T.B. Scott, *Mater. Sci. Eng. A* 635, 59 (2015).
11. S. He, H. Shang, A. Fernández-Caballero, A.D. Warren, D.M. Knowles, P.E.J. Flewitt, and T.L. Martin, *Mater. Sci. Eng. A* 807, 140859 (2021).
12. L.A. Avila Calderón, B. Rehmer, S. Schriever, A. Ulbricht, L. Agudo Jácome, K. Sommer, G. Mohr, B. Skrotzki, and A. Evans, *Mater. Sci. Eng. A* 830, 142223 (2022).
13. M. Li, X. Zhang, W.-Y. Chen, and T.S. Byun, *J. Nucl. Mater.* 548, 152847 (2021).
14. R.J. Williams, J. Al-Lami, P.A. Hooper, M.-S. Pham, and C.M. Davies, *Addit. Manuf.* 37, 101706 (2021).



15. C.D. Lundin, W.T. DeLong, and D.F. Spond, *Weld. J.* 54, 241 (1975).
16. Y.-H. Hsiao, Factors Affecting Creep Damage Accumulation and Mechanical Properties of 316 Stainless Steel Weldments, The Ohio State University, (1994).
17. J. Gonzalez, S. Tate, and J. Klemm-Toole, *JOM* 75, 4793 (2023).
18. A01 Committee, *Specification for General Requirements for Flat-Rolled Stainless and Heat-Resisting Steel Plate, Sheet, and Strip* (ASTM International, n.d.).
19. E28 Committee, *Test Methods for Tension Testing of Metallic Materials* (ASTM International, n.d.).
20. E28 Committee, *Test Methods for Elevated Temperature Tension Tests of Metallic Materials* (ASTM International, n.d.).
21. E01 Committee, *Test Method for Analysis of Austenitic Stainless Steel by Spark Atomic Emission Spectrometry* (ASTM International, n.d.).
22. E01 Committee, *Test Methods for Determination of Carbon, Sulfur, Nitrogen, and Oxygen in Steel, Iron, Nickel, and Cobalt Alloys by Various Combustion and Fusion Techniques* (ASTM International, n.d.).
23. E.P. Butler and M.G. Burke, *Acta Metall.* 34, 557 (1986).
24. M. Soleimani, A. Kalhor, and H. Mirzadeh, *Mater. Sci. Eng. A* 795, 140023 (2020).
25. M. Kamaya, *Mater Charact* 60, 125 (2009).
26. M.E. Kassner, *Fundamentals of Creep in Metals and Alloys*, 3. ed (Elsevier, Amsterdam [u.a.], 2015).
27. D.G. Morris and D.R. Harries, *Metal Sci.* 12, 525 (1978).
28. F. Dobeš and K. Milička, *Metal Sci.* 10, 382 (1976).
29. G.H. Eichelman and F.C. Hull, *Tran. Amer. Soc. Metals* 45, 77 (1953).
30. T. Angel, *J. Iron Steel Inst.* 177, 167 (1953).
31. K. Spencer, J.D. Embury, K.T. Conlon, M. Véron, and Y. Bréchet, *Mater. Sci. Eng. A* 387–389, 873 (2004).
32. O.D. Sherby and P.M. Burke, *Prog. Mater. Sci.* 13, 323 (1968).
33. *BPVC Section I-Rules for Construction of Power Boilers* (ASME, 2023).

**Publisher's Note** Springer Nature remains neutral with regard to jurisdictional claims in published maps and institutional affiliations.